International Journal of Hydrogen Energy 92 (2024) 544–559

Contents lists available at ScienceDirect

International Journal of Hydrogen Energy

journal homepage: www.elsevier.com/locate/he

Numerical simulation of hydrogen dispersion in an open-ended rectangular channel

H.E. Fossum [a,*], E. Åkervik [a], M. Henriksen [b], D. Bjerketvedt [b]

[a] Norwegian Defence Research Establishment (FFI), Instituttveien 20, Kjeller, 2007, Norway
[b] Faculty of Technology, Natural Sciences and Maritime Sciences, University of South-Eastern Norway, Kjølnes Ring 56, Porsgrunn, 3918, Norway

ARTICLE INFO

Keywords:
Hydrogen
Dispersion
CFD
Hydrogen leaks
Jet momentum length
Safety

ABSTRACT

In this work, large-eddy simulations of hydrogen dispersion from turbulent subsonic hydrogen-gas emissions in a $5.8 \times 0.9 \times 0.8$ m^3 open-ended channel are described. Such numerical modeling of hydrogen-related processes can provide new insights into the safety aspects of hydrogen, an increasingly more common energy carrier, particularly related to explosion hazards. Ten simulations, with jet mass flow rates ranging from 0.08 g/s to 1.27 g/s, have been simulated using the open-source OpenFOAM® 10 suite. The predicted concentrations in the channel are compared to corresponding experimental data, generally showing good agreement. Two distinct dispersion regimes are observed from the numerical data; a strongly stratified "filling box" regime is found for hydrogen mass flows $\lesssim 0.15$ g/s, whereas a more homogenized "fading box" regime emerges for higher mass flows. Based on the local Froude number in the channel, a novel model for the momentum length scale of the hydrogen jet is proposed, applicable to downward, strongly buoyant (i.e., non-Boussinesq) jets. It is demonstrated that the ratio of this length scale to the vertical length scale of the geometry can be used to predict the dispersion regime, which may benefit simplified predictive models for hydrogen concentrations and, consequently, ignition risks.

1. Introduction

As an energy carrier, hydrogen is becoming increasingly relevant as all sectors, including transportation, aim to reduce carbon emissions [1]. However, handling and storing hydrogen, whether in compressed-gas tanks, cryo-compressed tanks or cryogenic liquid tanks, are associated with significant safety concerns [2]. Several past accidents have resulted in human fatalities [3].

Numerical simulations of the physics associated with hydrogen-related processes can provide new insights into the safety aspects of hydrogen. Such processes include the release and dispersion of hydrogen, as well as potential ignition events, resulting in jet fires or deflagration/detonation incidents.

In recent decades, computational fluid dynamics (CFD) has become a valuable tool both in engineering and for academic research, particularly in combination with experimental work. CFD is well-suited to investigate parameter variations of a scenario, it allows for extensive data extraction, and it has a relatively low cost as well as virtually no related safety hazards.

Hydrogen releases can be divided into buoyancy-dominated leaks and momentum-dominated jets. The latter can be further subdivided into subsonic jets, in which the pressure ratio across the orifice is below a critical ratio ($p/p_{\mathrm{atm}} = 1.9$ for hydrogen), and underexpanded jets, resulting from choked flow at the orifice. An initially momentum-dominated jet will eventually transition to a buoyancy-dominated regime if it does not impinges on a wall or obstacle.

The HySafe and HyIndoor projects defined a range of benchmark problems for which experimental measurements and numerical simulations have been carried out [see, e.g.,4–6], typically using low release rates (less than $\sim$ 100 Nl/min or, equivalently, $\sim$ 0.14 g/s), i.e., well within the buoyancy-dominated plume regime and sometimes even laminar.

More recently, Bernard-Michel et al. [7] compared data from large-eddy simulations (LES) to particle image velocimetry (PIV) data for gas dispersion in a two-vented cavity, using helium and an extremely low flow rate (5 Nl/min or 0.007 g/s). Tolias et al. [8] provided the first publication of best-practice guidelines (BPGs) specifically for the numerical simulation of hydrogen dispersion. Ginaissi et al. [9] later demonstrated the practical application of the BPGs in simulations of a low-Re jet release of helium into an idealized parking-garage geometry, with acceptable results.

Other work includes that of Zhang et al. [10], who studied the natural gas ventilation from a hydrogen bus. Li et al. [11] investigated

* Corresponding author.
E-mail address: hannibal.fossum@ffi.no (H.E. Fossum).

https://doi.org/10.1016/j.ijhydene.2024.10.038
Received 12 July 2024; Received in revised form 8 September 2024; Accepted 4 October 2024
Available online 29 October 2024
0360-3199/© 2024 The Authors. Published by Elsevier Ltd on behalf of Hydrogen Energy Publications LLC. This is an open access article under the CC BY license (http://creativecommons.org/licenses/by/4.0/).

the effect of obstacles on the dispersion of hydrogen using numerical simulations, with release rates of ≈ 1000 Nl/min, i.e., ≈ 1.4 g/s. Xu et al. [12] studied hydrogen dispersion in a long channel experimentally and by means of Reynolds-averaged Navier–Stokes (RANS) simulations.

Resolving the dynamics of momentum-dominated jets is more computationally demanding; as the jet approaches choked flow through the nozzle, the demands on the spatio-temporal resolution increases dramatically. Under-expanded jets are associated with a complex series of shocks, including a Mach disk [13], forming downstream of the orifice. For resolved simulations of choked jets, shock-capturing schemes must be employed. Subsequent dispersion in the near-ambient conditions surrounding the jet occurs on much larger time scales and is usually modeled in a separate domain [see, e.g., 14,15].

Integral models provide a computationally cheaper alternatives to fully resolved jet simulations. The notional-nozzle concept is the most common model for under-expanded jets; originally proposed by Birch et al. [13], several variations and improvements have been published later [16–19]. Papanikolaou et al. [20] provide an evaluation of several such notional-nozzle approaches for hydrogen jet simulations. Li et al. [21] have extended the framework into a two-layer model.

Examples of hydrogen dispersion simulations utilizing the notional-nozzle model for safety evaluations are the work of Yu et al. [22], who considered a leakage from a fuel-cell vehicle, Qian et al. [23], where leakage from a refueling station was considered, and Hussein et al. [24], who simulated hydrogen emissions from a 700 bar storage container in a hydrogen-powered vehicle parked in a covered car park.

Integral models are also used for subsonic jets [25,26], and can be used to model the entire release and dispersion process, e.g., using the FRED [27] or HYRAM [28] model packages. Naturally, CFD and integral models can be used in combination [29,30].

In this paper, large-eddy simulations (LES) of dispersion from high-Reynolds number subsonic hydrogen-gas emissions in a semi-closed channel are documented. The channel dimensions are 5.8 ×0.9× 0.8 m^3. Hydrogen is injected from the ceiling and directed downwards, 0.5 m from the inner wall, and the channel is open in the opposite end. Injection rates from 0.084 to 1.25 g/s (i.e., from 60 to 900 Nl/min) have been simulated. The lowest mass rate results in a buoyancy-dominated leak, whereas the highest rate produces a momentum-dominated jet. Some of the simulations include geometric obstacles in the channel. The simulations are carried out using OpenFOAM®, and the results are analyzed and compared to experimental data [31,32].

OpenFOAM® is an open-source solver framework comprising multiple branches and sub-solvers. The software is implemented in the object-oriented C++ language and supports parallel processing. OpenFOAM® provides a range of discretization schemes and linear-system solvers. In this work, the *buoyantReactingFoam*[1] solver from OpenFOAM-10[2] has been used [see also33].

The aim of this study is partly to validate our computational methodology and partly to provide additional flow and dispersion data to aid the interpretation of the experimental measurements.

Following this introduction, Section 2 briefly summarizes the dispersion experiments used to generate reference data. Section 3 outlines our numerical method and parameters, including descriptions of the simulated cases and a mesh evaluation. The numerical results are discussed in Section 4; after an overview of the data as a whole, details from selected simulations are presented. We also provide different estimates of the jet momentum length scale and propose a new estimate for downward jets, based on a scaling law for the (mean) local Froude number. Finally, Section 5 provide a few concluding remarks.

[1] Adapted from *fireFoam*, an earlier version of the solver.

[2] https://doc.cfd.direct/openfoam/user-guide-v10/index

2. Experimental work

The exact inner dimensions of the 6-meter channel in the experiments match the numerical domain to be described shortly (Section 3.3). The floor, ceiling, and end wall were constructed of three U-profile steel beams bolted together. One of the side walls has all steel plates, whereas the other has two steel plates and four polycarbonate windows.

Hydrogen was injected at the top, 0.5 m from the closed end, and 0.45 m from the side wall of the channel. The inlet was circular with a diameter of 4.6 mm. The channel was outfitted with 29 hydrogen concentration sensors (XEN-5320 Xensors), with corresponding measurement points in our numerical simulations (see Fig. 1(b)).

In selected experiments, a wooden structure was placed 2.1 m from the closed end of the channel to obstruct the flow. This obstacle was 1 m long (y-axis), 0.8 m wide (z-axis), and 0.75 m in height (z-axis). Three different blockage ratios were studied in the experiments, one of which (36.8%) was also simulated numerically. The wooden structure was primarily placed in the channel to provide flame acceleration for ignited cases, the results of which are to be described in a separate manuscript.

The hydrogen mass flow rate was measured and controlled using a Coriolis mass flow meter to ensure reliability and accuracy of the results. The total release time was determined based on concentration trends reaching a steady-state concentration.

The open channel is described in more detail in Åkervik et al. [34], and the experiments are discussed in Henriksen et al. [31].

3. Numerical simulation

This section describes the governing equations implemented in *buoyantReactingFoam*, as well as the most important modeling assumptions and parameters used in our simulations.

We have used the LES framework, which has several advantages over Reynolds-averaged Navier–Stokes (RANS) models, including less demands on model-parameter tuning and the ability to predict minimum and maximum values of local, time-varying fields. The physical phenomenon of mixing is of particular importance in gas dispersion. Small-scale fluctuations play an important part in the mixing process, and LES generally predicts such fluctuations more reliably than RANS approaches [35]. Published comparisons between RANS and LES modeling of hydrogen dispersion indicate that LES performs as well or better than RANS [6,36–39].

3.1. Governing equations

In the following, $\overline{f}$ and $\widetilde{f} = \overline{f}/\overline{\rho f}$ denotes the filtered and filtered density-weighted f variable, respectively. Using this notation, the conservation equations for mass and momentum for a Newtonian fluid can be written, respectively,

$$\partial_t \overline{\rho} + \nabla \cdot (\overline{\rho}\widetilde{\mathbf{u}}) = 0, \tag{1}$$

$$\partial_t(\overline{\rho}\widetilde{\mathbf{u}}) + \nabla \cdot (\overline{\rho}\widetilde{\mathbf{u}}\widetilde{\mathbf{u}}) = -\nabla \overline{p_m} - (\mathbf{g}\cdot\mathbf{x})\nabla\overline{\rho} + \nabla \cdot \left(\mu_{\text{eff}}\left[\nabla\widetilde{\mathbf{u}} + (\nabla\widetilde{\mathbf{u}})^T - \frac{2}{3}(\nabla\cdot\widetilde{\mathbf{u}})\mathbf{I}\right]\right). \tag{2}$$

Here, $\partial_t = \partial/\partial t$ is the time derivative, ∇ is the spatial gradient operator, $\widetilde{\mathbf{u}}$ is the velocity field, $\overline{\rho}$ is the density field, $\mathbf{g}$ is the gravitational acceleration, $\mathbf{x}$ is the position vector, t is the time variable, and $\mathbf{I}$ is the identity matrix. The effective viscosity is defined as $\mu_{\text{eff}} = \mu + \mu_{\text{sgs}}$, where μ is the dynamic (molecular) viscosity, calculated by Sutherland's viscosity law, and μ_{sgs} is the subgrid-scale viscosity, where a Boussinesq-type model for the subgrid-scale stress tensor is implicitly implied. In our simulations, the wall-adapting local-eddy viscosity model (WALE) of Nicoud and Ducros [40] with a model constant of $C_w = 0.325$ was used to model μ_{sgs}.

To improve convergence of the numerical solution, *buoyantReactingFoam* uses a modified pressure in Eq. (2), defined as

$$\overline{p_m} = \overline{p} - \overline{\rho}\mathbf{g}\cdot\mathbf{x}, \tag{3}$$

where $\overline{p}$ is the thermodynamic pressure and $\overline{\rho}\mathbf{g}\cdot\mathbf{x}$ is the hydrostatic pressure.

The thermodynamic properties of the gas are related through the ideal-gas equation-of-state (EOS), $\overline{\rho} = \overline{p}/(R_s\widetilde{T})$, where $\widetilde{T}$ is the temperature and R_s is the specific gas constant of the mixture, related to the universal gas constant, R, by $R_s = (Y_{\text{air}}/M_{\text{air}} + Y_{\text{H2}}/M_{\text{H2}})R$. Here, M_{air} and M_{H2} are the molar masses and Y_{air} and Y_{H2} the mass fractions of air and hydrogen, respectively.

Only two (inert) species are used in our simulations, i.e., hydrogen (H_2) and air. *buoyantReactingFoam* solves a transport equations for the mass fraction of H_2:

$$\partial_t(\overline{\rho}\widetilde{Y_{\text{H2}}}) + \nabla\cdot\left(\overline{\rho}\widetilde{\mathbf{u}}\widetilde{Y_{\text{H2}}}\right) = \nabla\cdot\left(\overline{\rho}D_{\text{eff}}\nabla\widetilde{Y_{\text{H2}}}\right), \tag{4}$$

whereas the mass fraction of air by definition is $Y_{\text{air}} = 1 - Y_{\text{H}_2}$. In Eq. (4), D_{eff} is the effective diffusivity, i.e., the sum of the mass diffusivity of hydrogen in air and the subgrid-scale diffusivity. The molecular diffusivity follows from Sutherland's thermal diffusivity law, assuming a unity Lewis number, and the sub-grid turbulent diffusivity is computed from the sub-grid viscosity assuming a unity turbulent Schmidt number.

Sensible enthalpy, $\widetilde{h}_s$, is used in the formulation of the energy conservation equation, i.e.,

$$\partial_t(\overline{\rho}\widetilde{h}_s) + \nabla\cdot\left(\overline{\rho}\widetilde{\mathbf{u}}\widetilde{h}_s\right) + \partial_t(\overline{\rho}K) + \nabla\cdot\left(\overline{\rho}\widetilde{\mathbf{u}}K\right) = \partial_t\overline{p} + \nabla\cdot\left(\overline{\rho}\alpha_{\text{eff}}\nabla\widetilde{h}_s\right), \tag{5}$$

where α_{eff} is the effective thermal diffusivity, again following from the Sutherland diffusivity law and the sub-grid viscosity, assuming a unity turbulent Prandtl number. $K = |\widetilde{\mathbf{u}}|^2/2$ is the kinetic energy. Viscous dissipation is considered a negligible heat source, given the generally low Mach number of our cases [41, p. 364].

In the opinion of the authors, the energy equation should contain an additional potential energy term, $\rho\mathbf{g}\cdot\mathbf{u}$, to be compatible with momentum conservation. After the simulations were finished, we realized that the implementation in *buoyantReactingFoam* lacks this term. However, selected cases (A and E, cf. Section 3.3) were compared to new simulations using a patched code that included the potential energy term. The differences in results were negligible. In the following, we therefore report the results from the original *buoyantReactingFoam* code.

The constant-pressure specific heat capacity ($C_{p,i}$) and sensible enthalpy ($h_{s,i}$) for each component in the gas mixture are related to the local temperature by polynomial expressions, often referred to as the NASA-7 polynomials [42]. Coefficients were calculated by the *mech2Foam* script [43] with the GRI-MECH 3.0 chemical-reaction mechanism [44]. The mixture enthalpy is calculated from the volume-weighted average of the component enthalpies.

3.2. Computational setup

We have tried to adhere to existing best-practice guidelines for hydrogen-dispersion simulations, discussed in Tolias et al. [8], as much as possible. Deviations from the recommendations, in particular regarding the choice of Courant number, are discussed below.

buoyantReactingFoam uses OpenFOAM's PIMPLE pressure–velocity coupling, which is a combination of the Pressure-Implicit Splitting of Operators (PISO) and Semi-Implicit Method for Pressure-Linked Equations (SIMPLE) algorithms. *buoyantReactingFoam* is a solver for compressible flows without the presence of shocks, i.e., typically suitable for Mach numbers below unity. In our case, one outer solution loop and two inner loops were employed at each time step, effectively reducing the algorithm to a PISO coupling.

Choosing an appropriate time step is not straight-forward for simulations with narrow, high-speed jets, due to the large velocities and small mesh cells in the vicinity of the hydrogen inflow. We have used a local Courant number requirement of $\text{Co} = U\Delta t/\Delta x \leq 300$, where U is a measure of the local velocity scale and Δt and Δx are the temporal and (local) spatial resolutions, respectively. For case H, $\text{Co} \leq 150$ was required for stability, due to extreme flow velocities near the inlet. Only a few cells close to the hydrogen inflow will approach the maximum Courant number; most cells ($\geq$ 90 %) satisfy $\text{Co} < 0.1$ in all our simulations. The average Courant number (in space and time) was < 0.01 for all the simulations we report here.

The very small time step enabled the use of first-order temporal discretization, i.e., implicit Euler integration, to increase stability and speed up the simulations. All spatial gradients are computed using Gauss' theorem with cell-based linearly interpolated face fluxes. The diffusion terms have been discretized by central differencing. The momentum advection term was discretized by blending 75% central differencing and 25% upwinding to increase stability. We employed a total-variation diminishing (TVD) scheme (OpenFOAM's `limitedLinear 1`) for the advection of mass fractions and energy.

The pressure equation was solved by the generalized geometric-algebraic multigrid method (GAMG) combined with a Gauss–Seidel smoother. The preconditioned biconjugate gradient stabilized method (PBiCGStab) was used to solve the discretized equations for momentum, species transport and energy. The linear systems were preconditioned by the simplified diagonal-based incomplete LU preconditioner (DILU).

The boundary conditions for velocity ($\widetilde{\mathbf{u}}$), modified pressure ($\overline{p_m}$), mass fractions ($\widetilde{Y_i}$) and temperature (T) are listed in Table 1. For the modified pressure, the *totalHydrostaticPressure* condition uses a precomputed hydrostatic pressure field at the boundary as a target total pressure, leading to a varying static pressure according to the local flow (i.e., dynamic pressure) variation. In *buoyantReactingFoam*, wall models are incorporated via the kinematic viscosity, $\nu_{\text{sgs}} = \mu_{\text{sgs}}/\overline{\rho}$. We have used the wall model based on Spalding's wall law [45]. All the *inletOutlet*-type conditions impose a zero-gradient condition for flow out of the boundary and a fixed-value condition in the case of reversed flow.

3.3. Case descriptions

As shown in Fig. 1(a), y is taken as the flow along the channel and z is the vertical direction (positive in the opposite direction of gravity). The computational domain was set up to match the experimental study as closely as possible. The domain comprises a rectangular channel of $(L_x, L_y, L_z) = 0.9 \times 5.8 \times 0.8$ m^3 that is closed in the rear end ($y = 0$) and opens (at $y = 5.8$ m) into a larger region with an extended vertical expansion, to minimize effects from the outlet boundaries. In some of the experiments, and hence in some of our simulations, a geometric obstruction was inserted into the channel, partially blocking the flow with a blockage area ratio of 36.8%.

Fig. 1 illustrates the computational domain and the experimental measurement setup.

H_2 is injected through an approximately circular opening with diameter $D_{\text{in}} = 4.6$ mm in the channel ceiling, at $y = 0.5$ m. In the experiment, 29 hydrogen sensors were used to measure and record the hydrogen concentrations in time, located as shown in Fig. 1(b). The top sensors (blue) are placed on the channel ceiling, the top-middle sensors (red; 03, 05, 08, 13, 18) are placed 28 ± 0.5 cm from the ceiling, the bottom-middle sensors (red; 23, 24, 26, 28, 29) are placed 28 ± 0.8 cm from the floor, and the bottom sensors are placed on the floor [31,32]. We have extracted hydrogen concentrations in time from our simulations at the corresponding locations in the computational domain.

The simulated mass flows of injected hydrogen varied between 0.086 and 1.27 g/s, cf. Table 2. The table lists the corresponding inlet Mach number (assuming room temperature and pressure, as well as

Table 1
Boundary conditions for velocity ($\widetilde{\mathbf{u}}$), modified pressure ($\overline{p_m}$), mass fractions ($\widetilde{Y}_i$) and temperature (T). Specific fixed values are shown in parentheses where relevant.

	Inlet	Far-field	Walls
$\widetilde{\mathbf{u}}$	flowRateInletVelocity	pressureInlet-OutletVelocity	noSlip
$\overline{p_m}$	fixedFluxPressure	prghTotal-HydrostaticPressure	fixedFluxPressure
$\widetilde{T}$	fixedValue (293)	inletOutlet	fixedValue (293)
$\widetilde{Y}_i$	fixedValue (air: 0; H_2: 1)	inletOutlet	zeroGradient
ν_{sgs}	calculated	calculated	nutUSpalding-WallFunction

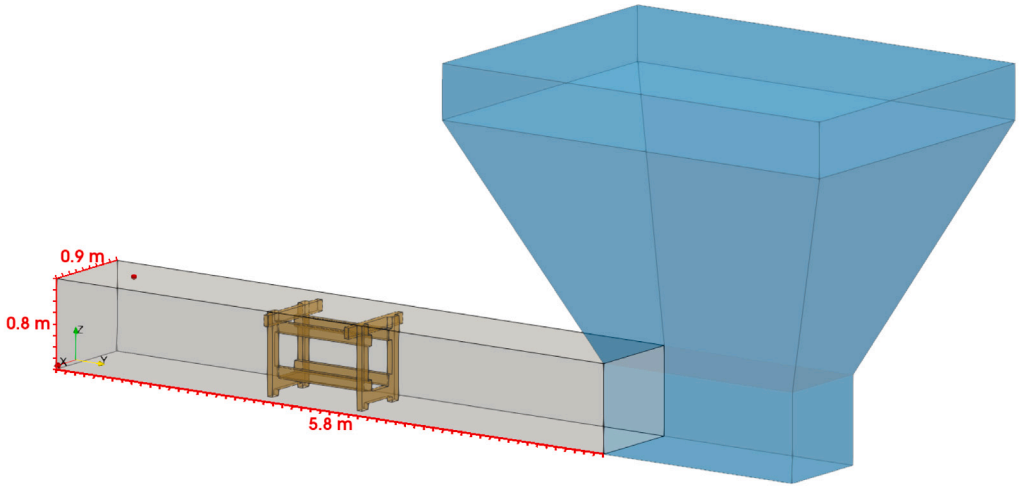

(a) A perspective illustration of the computational domain. The inlet position is marked with a red dot, and the ambient boundary is shown in blue. The geometrical obstruction (shown in orange) is only included in cases O1 and O2, cf. Table 2).

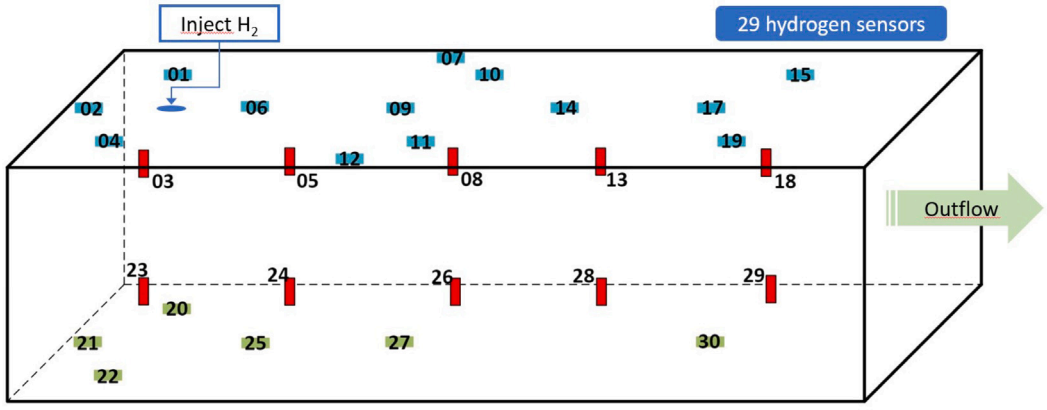

(b) The placement of the hydrogen sensors in the experimental measurements.

Fig. 1. The open-ended channel. (For interpretation of the references to color in this figure legend, the reader is referred to the web version of this article.)

uniform velocity across the inlet) for the hydrogen injection.[3] The three right-most columns list data related to the mesh resolution, discussed in Section 3.4.

The two last cases (O1 and O2) include the geometrical obstruction shown in Fig. 1(a). This obstruction, as well as others, was included in the experiments mainly to increase flame area and subsequent deflagration pressures in the combustion experiments. We simulated two cases with an obstruction to verify that *buoyantReactingFoam* produces reliable results for these more complex geometries.

In addition to the cases in Table 2, simulations were carried out to investigate our choices of mathematical and numerical models. This included other turbulence and wall models, face flux interpolation schemes, temporal discretizations (up to second order), reduced maximum Courant number ($\lesssim 100$) and different implementations of the pressure boundary condition. Some of these changes also required an increased number of corrector loops in the pressure–velocity coupling algorithm. In general, the simulation results were relatively unaffected by the changes in numerical parameters. Tests with the Reynolds-Averaged Navier–Stokes (RANS) k-ω SST turbulence model produced overall inferior results when compared to experimental data.

[3] The speed of sound is taken as $c = 1270$ m/s [46].

Table 2
Injected H_2 mass flow ($\dot{m}$ [g/s]), injection Mach number (Ma), jet Froude number (Fr_j), average l_+ and R_k, and the fraction of cells with more than 80% resolved energy ($C_{R_k \geq 0.8}$) for all the simulations. Where available, reference data are taken from [32].

Case	Reference case	$\dot{m}$	Ma	Fr_j	Avg. l_+	Avg. R_k	$C_{R_k \geq 0.8}$
A	Test 02-0a/b	0.086	0.05	79	8.0	0.96	0.999
B	–	0.15	0.09	138	12.1	0.96	0.998
C	–	0.20	0.11	185	15.1	0.95	0.998
D	–	0.30	0.17	277	17.2	0.95	0.996
E	Test 05-0a/b	0.48	0.27	443	20.3	0.94	0.995
F	Test 07–0	0.74	0.42	683	23.9	0.94	0.997
G	–	1.00	0.57	923	27.2	0.94	0.997
H	Test 08–0	1.27	0.72	1172	30.2	0.93	0.996
O1	Test 02-1a/b	0.091	0.05	84	7.6	0.95	0.988
O2	Test 05-1a/b	0.45	0.26	415	18.7	0.93	0.988

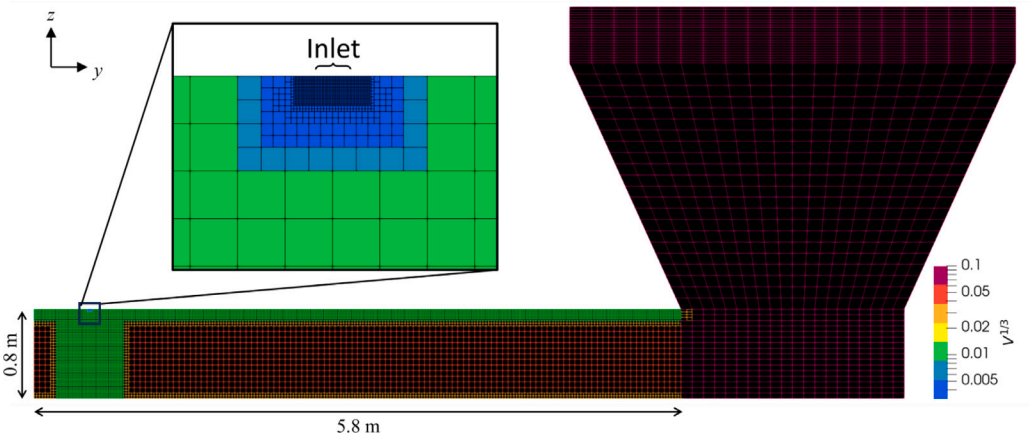

Fig. 2. The computational mesh in a vertical midsection ($x = 0$) of the domain. Inset shows a close-up of the injection region.

3.4. Mesh assessment

Our computational mesh consists of 494,468 cells, with cell-edge lengths within the channel ranging from $3.90625 \cdot 10^{-4}$ m at the hydrogen inlet to 0.05 m far away from the hydrogen jet.[4] In addition to the refinement at the inlet, we used a refinement zone in the jet region and near the ceiling, where the cells have edge lengths of 0.0125 m. Local mesh refinement occurs by 1-to −2 edge splitting. A vertical slice at $x = 0$ is shown in Fig. 2.

The cases with geometrical obstructions comprise a mesh of 542,466 cells, with refinement to 0.0125 m near the surfaces of the obstruction.

The mesh is hexahedral and based on a cut-cell approach. In the entire channel, the mesh is orthogonal with zero skewness and a unity aspect ratio.[5] The edge of the injection zone is a staircase approximation of a circle, resulting in a simulated injection area 2.5% larger than for the corresponding nominal injection orifice in the experiments.

Large-eddy simulations with implicit filtering are ill-suited for classical mesh convergence studies, since the momentum equation depends explicitly on the mesh size through the subgrid-scale viscosity. Thus, the turbulence model itself changes with the mesh resolution. Within certain resolution ranges, increased resolution may even increase the total error [47]. Instead of an evaluation of mesh convergence, we will therefore consider the estimated ratio of resolved to total kinetic energy and the estimated viscous length scales per cell to assess our mesh.

The resolved turbulence kinetic energy is given by $k_{\text{res}} = \frac{1}{2}\langle \mathbf{u}' \cdot \mathbf{u}' \rangle$, where $\langle \cdots \rangle$ denotes a suitable averaging process and $\mathbf{u}' = \widetilde{\mathbf{u}} - \langle \widetilde{\mathbf{u}} \rangle$. Ideally, an ensemble average is applied, but system ergodicities can allow for other averaging procedures [48, p. 34]. We use a temporal average from $t = 60$ s to $t = 120$ s. The subgrid kinetic energy, formally defined as $k_{\text{sgs}} = \frac{1}{2}\langle (\mathbf{u} - \widetilde{\mathbf{u}}) \cdot (\mathbf{u} - \widetilde{\mathbf{u}}) \rangle$, is estimated by *buoyantReactingFoam* from subgrid length and velocity scales in the WALE model. Consequently, the estimated ratio of resolved to total turbulence kinetic energy can be written

$$R_k = \frac{k_{\text{res}}}{k_{\text{res}} + k_{\text{sgs}}}$$

The viscous (or Kolmogorov) length scale, where kinetic energy is dissipated into thermal energy, is defined as $\eta = (\nu^3/\epsilon)^{1/4}$, where $\nu = \mu/\rho$ and ϵ are the kinematic viscosity and turbulence dissipation rate, respectively. Consequently, $l_+ = \Delta/\eta$, where Δ is the mesh resolution, quantifies the number of viscous length scales per computational cell length [49]. Since the dissipation rate is unknown, l_+ must be estimated from resolved scales and dimensional arguments. Here, we use the estimate

$$l_+ = \left\langle V^{1/3} \sqrt{\bar{\rho} \widetilde{S} / \mu} \right\rangle,$$

in which V is the cell volume and $\widetilde{S} = \sqrt{2(\nabla \widetilde{\mathbf{u}} + (\nabla \widetilde{\mathbf{u}})^T)}$ is a measure of the (resolved) strain rate. Near the walls, the l_+ estimate approaches an approximation of the more common y_+ estimate.

Table 2 lists the mean values of R_k and l_+ within the channel, as well as the fraction of cells in the channel with more than 80% resolved energy ($C_{R_k \geq 0.8}$). Unexpectedly, the relative mesh quality degrades with increasing mass flow of injected hydrogen, leading to less resolved energy and larger values of l_+.

Histograms for the local cell values of R_k for cases A, E and H (cf. Table 2) are presented in Fig. 3. Cases A and H exhibit the lowest and highest flow velocities, respectively, thus yielding the best and poorest mesh qualities relative to the flow field (since all cases are simulated on the same mesh). Case E is close to a median case in terms of the hydrogen injection rate.

[4] In the ambient region outside the channel outlet, the largest edge length was 0.2 m near the top boundary.

[5] The mesh in the region outside of the channel exhibits slight skewness and non-orthogonality.

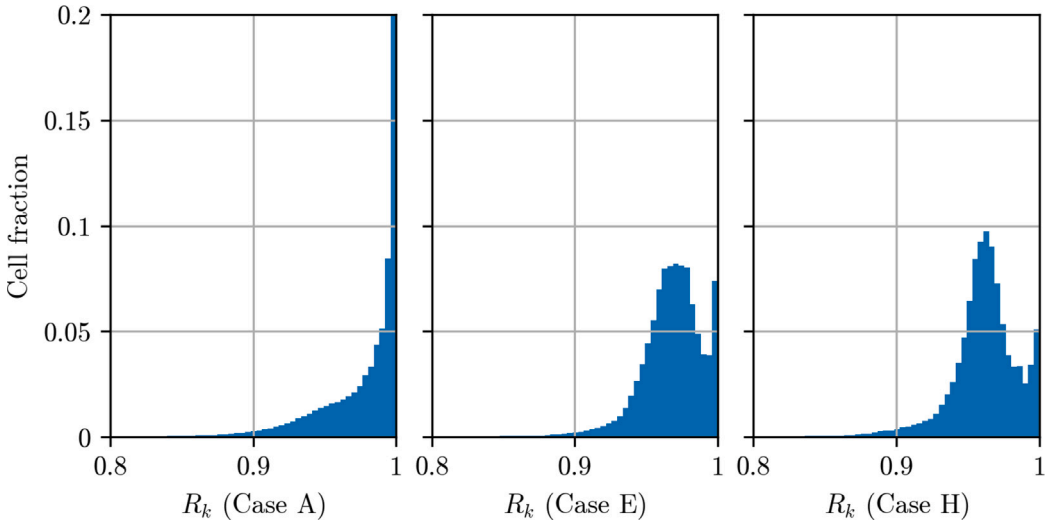

Fig. 3. R_k histograms for cases A (left), E (middle), and H (right). $R_k = 1$ implies that all turbulence kinetic energy is resolved.

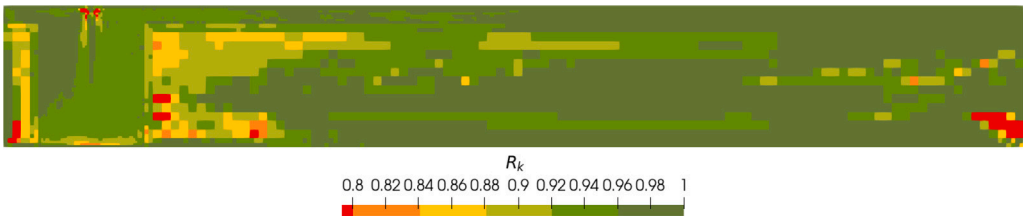

Fig. 4. Cell values of R_k in a vertical cut-plane at $x = 0$ for case E.

A typical quality criteria used in LES is that the resolved energy ratio should satisfy $R_k \geq 0.8$ [50]. As seen in Table 2 and Fig. 3, our mesh satisfy this criteria both globally and locally, with the exception of a few cells.

The spatial variation of R_k in a vertical slice ($x = 0$) for case E is shown in Fig. 4. Generally, the local values of R_k are high (mostly above 90%), as expected from the agglomerated statistics. This is also the case inside of the hydrogen jet.

The main drawback of our mesh is the inability to accurately resolve parts of the edges of the hydrogen jet (and the jet impingement region at the channel floor). This is exemplified by the regions of $R_k < 0.8$ in Fig. 4, both very close to the inlet and directly outside of the jet refinement region, where the flow shear is still rather high.

We performed test simulations on meshes with higher spatial resolutions, but the required temporal resolution for such meshes was too computationally demanding.

In the final part of this section, we will compare simulation data to experimental measurements. In the cases where two reference data sets exist (*a* and *b*, cf. Table 2), averages of the two sets are used. Fig. 5 shows scatter plots for cases A, E, F, H, O1 and O2. The relationship between simulated mean hydrogen concentrations and corresponding experimental measurements are shown for all sensor locations used in the experiments. The temporal averaging is discussed further in Section 4.

In general, Fig. 5 indicates a good agreement between measured data and numerical predictions for different H_2 mass flows. Most data pairs exhibit less than 25% difference. *buoyantReactingFoam* seems to give acceptable predictions even for relatively high nozzle Mach numbers (cases F and H), as well as for more complex geometries (cases O1 and O2).

For the low-rate injections (cases A and O1), *buoyantReactingFoam* appears to under-predict the highest concentrations, whereas for the high-rate injections (cases E, F, H, and O2), *buoyantReactingFoam* over-predicts the lower concentrations.

3.4.1. Statistical evaluation

Through the process of statistical evaluation, key aspects of how predicted data compares to reference data can be quantified. A multitude of metrics exist to measure the degree of data overlap, bias, scatter or correlation [see, e.g.,51].

Two common metrics that quantifies relative bias and scatter are given by the fractional bias (FB) and the normalized mean square error (NMSE), respectively. They can be calculated from "predicted" (i.e., numerically simulated) and "observed" (i.e., experimentally measured) data:

$$\mathrm{FB} = \frac{\langle C_o \rangle - \langle C_p \rangle}{0.5(\langle C_o \rangle + \langle C_p \rangle)},$$

$$\mathrm{NMSE} = \frac{\langle (C_o - C_p)^2 \rangle}{\langle C_o \rangle \langle C_p \rangle},$$

where C_p and C_o denote predicted and observed data, respectively. Here, the averaging procedure denoted by $\langle \cdots \rangle$ is simply an arithmetic average over the dataset. The FB measures the systematic deviation of the predicted data from the observed data; a positive value indicates an *under*-prediction. A perfect prediction implies that FB = NMSE = 0.[6]

In the case of data with a wide value range, the geometric bias (MG) and geometric variance (VG) are often recommended to give a more balanced treatment of extreme values:

$$\mathrm{MG} = \exp(\langle \ln C_o \rangle - \langle \ln C_p \rangle)$$

$$\mathrm{VG} = \exp\left(\langle (\ln C_o - \ln C_p)^2 \rangle\right)$$

However, this comes with the caveat that data values approaching zero must be thresholded to avoid adversely affecting the results (MG and

[6] From the definition of FB, it follows that $\langle C_p \rangle / \langle C_o \rangle = (1 - 0.5\mathrm{FB})/(1 + 0.5\mathrm{FB})$. Hence, a fractional bias of, e.g., 0.5 implies a mean under-prediction of 40%.

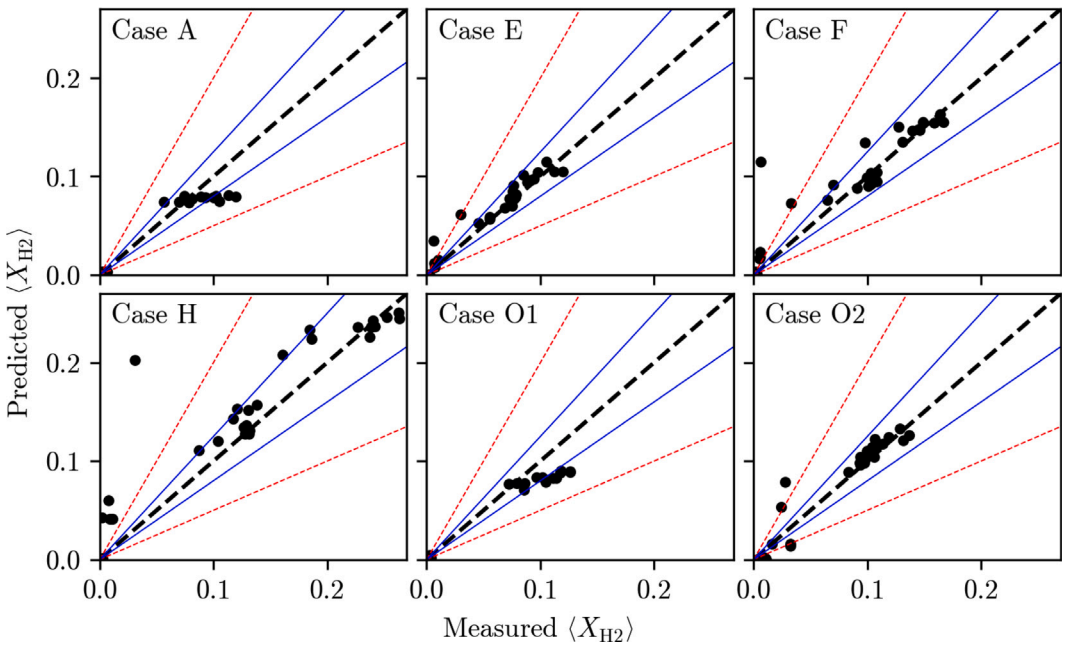

Fig. 5. The relationship between measured (x-axis) and simulated (y-axis) mean hydrogen volume fractions, $\langle X_{H2} \rangle$, for cases A, E, F, H, O1, and O2. $x = y$ (heavy dashed line) indicates perfect correlation. Blue solid lines and dashed red lines indicate data ratios of 1.25 and 2, respectively. (For interpretation of the references to color in this figure legend, the reader is referred to the web version of this article.)

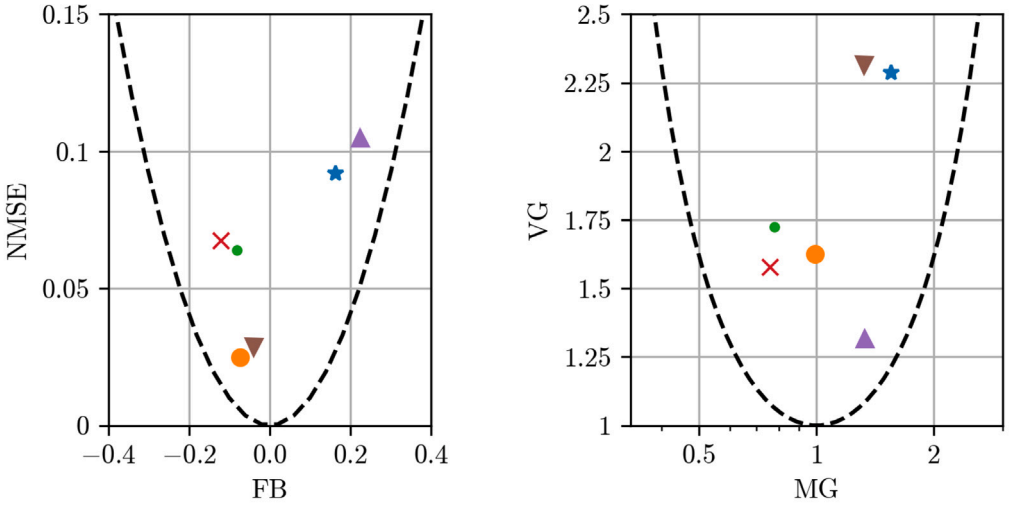

(a) Normalized mean square error vs. fractional bias.

(b) Geometric variance vs. geometric mean bias. The x-axis is logarithmic.

Fig. 6. Statistical evaluation metrics comparing numerically predicted and experimentally measured mean concentration values for cases A (⋆), E (•), F (·), H (×), O1 (▲), and O2 (▼). The pure-bias curves, Eq. (6), are also shown (- -). (For interpretation of the references to color in this figure legend, the reader is referred to the web version of this article.)

VG are undefined for zero values). The MG measures the systematic ratio between the predicted and observed data; $MG > 1$ implies an *under*-prediction. In the case of perfect prediction, MG = VG = 1 .

NMSE and VG incorporate both systematic and random errors in the predicted data. However, following Chang and Hanna [51], the systematic component can be explicitly extracted in both cases. The resulting equations give the minimum NMSE and VG values for given values of the FB and MG, assuming a systematic bias only. These pure-bias curves are given, respectively, by

$$\mathrm{NMSE}_s = \frac{4\,\mathrm{FB}^2}{4 - \mathrm{FB}^2}, \qquad \mathrm{VG}_s = \exp((\ln \mathrm{MG})^2) \tag{6}$$

and it is thus NMSE − NMSE_s and VG − VG_s that measures the unbiased (random) error in the data.

We computed four metrics (FB, NMSE, MG, VG) based on 29 sensors for six different cases (A, E, F, H, 01, 02). For the MG/VG calculations, we have used a value threshold of 0.2% mean concentration by volume for the experimental data. This resulted in the exclusion of 9 out of 29 points in cases A and O1.

Fig. 6 shows the statistical evaluation metrics for our simulations. The predicted and observed data are represented by simulated and measured mean hydrogen concentrations at each of the sensor locations in Fig. 1(b). In the cases where two reference data sets exist (*a* and *b*, cf. Table 2), averages of the two sets are used.

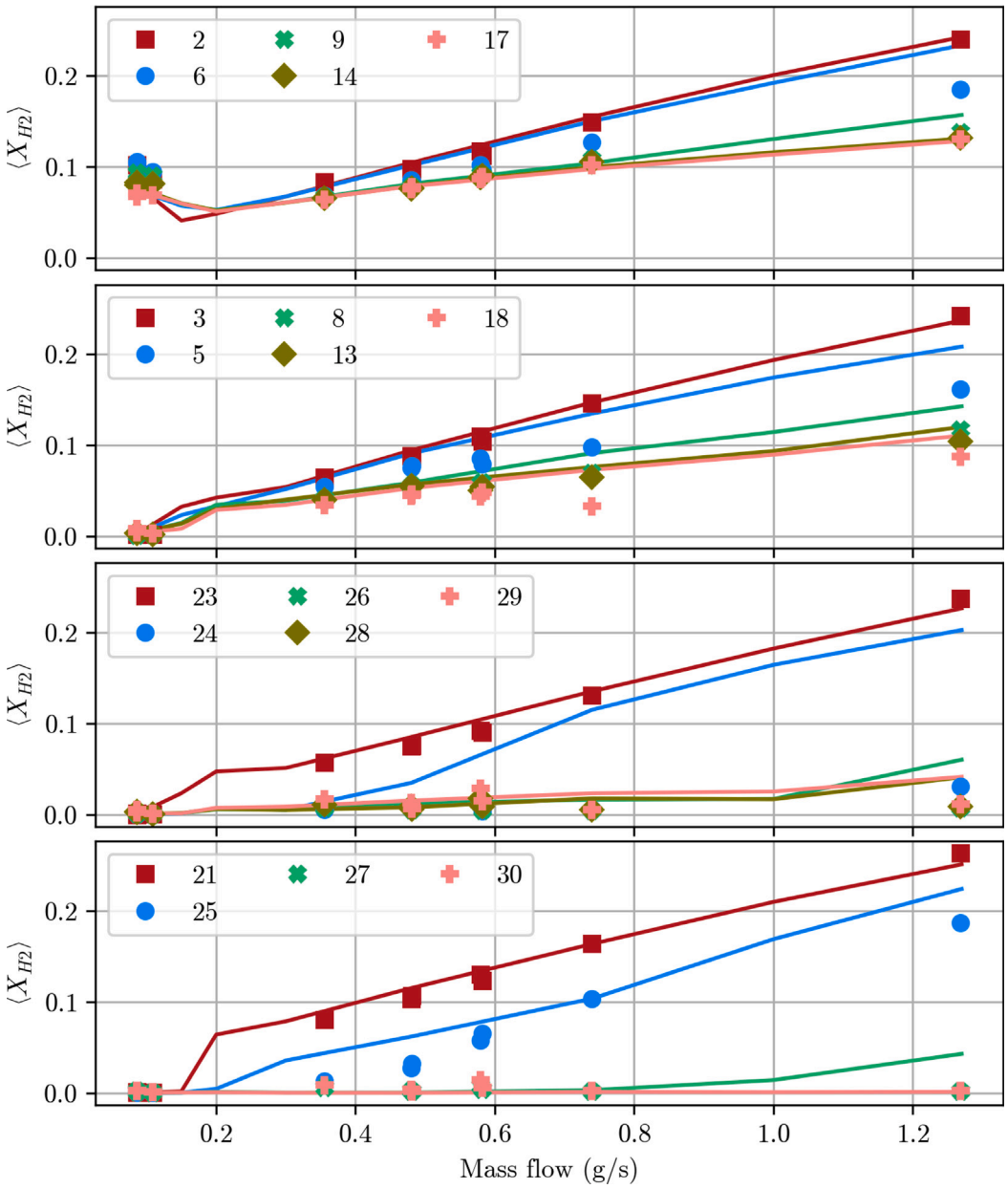

Fig. 7. Mean H_2 volume fraction as a function of inlet mass flow for different sensors, cf. Fig. 1(b). Marker symbols and colors are listed in individual legends; both experimental data (symbols only) and numerical data (lines with the same color as the corresponding experimental sensor symbol) are shown. (For interpretation of the references to color in this figure legend, the reader is referred to the web version of this article.)

Depending on the requirements and context of a model, different quality criteria are used for the evaluation metrics. It has been suggested [52] that models used for air quality predictions were acceptable for research-grade experiments if $-0.3 < FB < 0.3$ (or $0.7 < MG < 1.3$) and NMSE < 0.5 (or $VG < 1.6$). Giannissi et al. [9] recommended stricter criteria when evaluating indoor dispersion ($-0.18 < FB < 0.23$, NMSE < 0.05, $0.83 < MG < 1.25$), $VG < 1.05$). Since the experiments were performed in a semi-open channel and thus subjected to some degree of ambient wind, they cannot be considered fully indoor. Henriksen et al. [53] reported criteria for assessing deflagration models, where the model performance was considered excellent for $0.7 < MG < 1.3$, $VG < 1.6$ and acceptable if $0.5 < MG < 2$, $VG < 3.3$.

It is evident from Fig. 6 that our simulations produce predictions of mean concentrations well within acceptable limits. Both the bias and scatter are relatively low, with the most extreme cases (i.e., very low or very high mass flows) giving the poorest data quality. The statistical over-/underpredictions captured by the FB and MG corroborate the trends in Fig. 5, discussed earlier.

4. Results

4.1. Overview

The time-averaged concentrations for all simulations listed in Table 2 are shown in Fig. 7 as functions of the mass flow of injected hydrogen. The experimental tests are also included, except Test 05-0-c, which was considered an invalid outlier.

The simulation results are shown with colored lines, whereas all experimental data are shown in corresponding colors, but using symbols. The figure is split into four subfigures, each showing data from sensors at one specific height in the channel, cf. Fig. 1(b).

As will be shown shortly, all simulations were found to be statistically steady after 60 s. Thus, time averaging was employed from 60 to

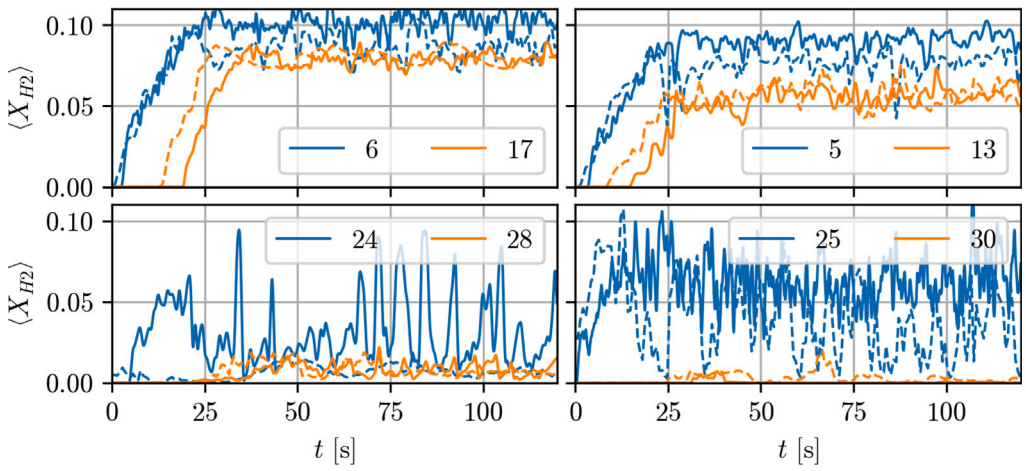

Fig. 8. Time history from selected hydrogen sensors from one simulation (case E; solid lines) and corresponding experiment (Test 05-0b; dashed line). $t = 0$ is taken as the beginning of the release. Data from two top (upper left), two medium-high (upper right), two medium-low (lower left), and two bottom (lower right) sensors are shown. For improved visibility, the simulation data shown here is filtered by a 5th-order Savitzky–Golay filter with a window of 200 samples.

120 s in all simulations to obtain mean values. The averaging period for each experiment was determined from mass-flow data and varied between experiments; we use the values computed in [31].

The data shown in Fig. 7 indicates a transition point around 0.2 g/s, particularly noticeable for the top and bottom sensors. Hydrogen injection rates higher than 0.2 g/s yield increasingly higher hydrogen concentrations at all locations in the channel. For mass flows below 0.2 g/s, no hydrogen is detected at all at the floor. However, near-ceiling concentrations actually increase.

The vertical hydrogen jet is directed downward, so the initial momentum of the flow acts in opposition to the significant buoyancy of hydrogen. For very low injection rates, buoyancy quickly overcomes the initial momentum, transporting hydrogen back to the top of the channel. As the injection rate increases, the increased momentum of the jet carries hydrogen further towards the bottom of the channel, thus reducing concentrations near the ceiling, until the mass flow is large enough, i.e. ≥ 0.2 g/s, aided by increased mixing induced by the turbulent jet, to increase concentrations in the entire channel.

Buoyant dispersion in confined spaces can be divided into two regimes, depending on the Morton number for forced buoyant plumes in confined spaces as defined by Denisenko et al. [54],

$$\mathrm{Mo} = l_s / H, \tag{7}$$

where l_s is a jet momentum length scale and H is the channel height. For $\mathrm{Mo} < 1$, the dispersion regime is buoyancy-dominated and the hydrogen concentration will be stratified, also known as the "filling box" model [55]. For $\mathrm{Mo} \geq 1$ turbulent mixing significantly homogenizes the hydrogen concentration and the dispersion is thus in a more momentum-influenced regime, known as the "fading box" model.

The choice of the momentum length scale, i.e. the length beyond which the jet is buoyancy-dominated, is not straight-forward. We will revisit the Morton number shortly (see Section 4.3), but Fig. 7 indicates that we have dispersion both in the "filling box" (mass flows $\lesssim 0.2$ g/s) and "fading box" (mass flows $\gtrsim 0.2$ g/s) regimes.

Fig. 7 corroborates the main conclusions of Section 3.4; generally, the CFD results are in good agreement with the experiments. However, the exact edge of the jet is difficult to predict accurately; sensors 5, 6, and 24 – which are all located near the jet shear edge (cf. Fig. 1(b)) – show significantly larger deviations than the other sensors.

4.2. Temporal evolution and mean concentration field

Examples of the temporal evolution of the hydrogen concentrations at different locations in the channel (cf. Fig. 1(b)) are shown for case E in Fig. 8. After a ramp-up period of approximately 30 s, the concentration values reaches a statistically steady state, although with persistent fluctuations in the signal.

There is considerable variation between the typical concentration levels at different positions; generally, sensors higher up and further from the open end of the channel exhibit higher concentrations.

Sensor 25 is greatly affected by the highly turbulent flow regime associated with jet impingement and thus exhibits more pronounced concentration fluctuations than other sensors, captured both in the experiments and the simulations. In the simulation data, sensor 24 also shows a significant level of fluctuations, but this is not found in the experimental data. Most likely, this is because the sensor is close to the jet edge and thus highly sensitive to the exact width of the jet; the simulated jet seems to be a bit wider than the jet in the experiments, perhaps due to excess numerical diffusion.

Although the agreement in the initial transient of the hydrogen dispersion is not perfect, the trends in concentration evolution are similar. In particular, sensors 5, 6, 13 and 17 all show approximately equal time derivatives in the build-up of concentration — though at slightly different delays for sensors 13 and 17.

The structure of the hydrogen dispersion is indicated from the concentration contours in Fig. 9, where instantaneous and mean volume concentrations from cases A, E and O2 are shown. The figure corroborates the data already discussed; hydrogen is initially transported downwards by the jet momentum. The inner end of the channel (between the inner wall and the jet) is relatively well mixed for the high momentum-cases (E and O2). In the outer part of the channel (between the jet and the open exit), buoyancy transports hydrogen towards the ceiling, yielding a vertical concentration gradient which depends on the injected mass flow.

Case A shows a thin high-concentration region near the ceiling, corresponding to a "filling box" dispersion regime. For case E, turbulent mixing results in a significantly more gradual transition between air and hydrogen, i.e., in line with the "fading box" regime.

The comparison of case E and O2 reveals that while the presence of a geometric obstruction alters the dispersion visibly, it does not instigate a fundamental change in the dispersion regime. Broadly, the effect appears to be a containment of more hydrogen in the inner parts of the channel and a subsequent thinner vertical layer of hydrogen in the outer parts, i.e., the resulting gravity current is altered somewhat by the obstruction.

The overall structures of the instantaneous concentration fields closely resemble those of the mean fields. This is also noticeable within the obstruction in case O2, where the upward transport of hydrogen seems to increase relative to the streamwise transport.

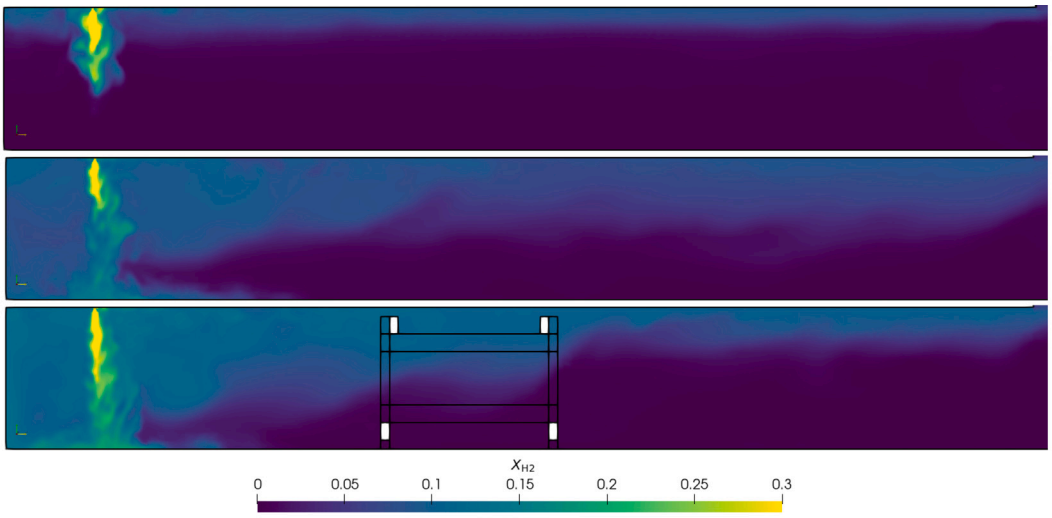

(a) Instantaneous ($t = 120$ s) concentrations, X_{H2}, for cases A (top), E (middle) and O2 (bottom).

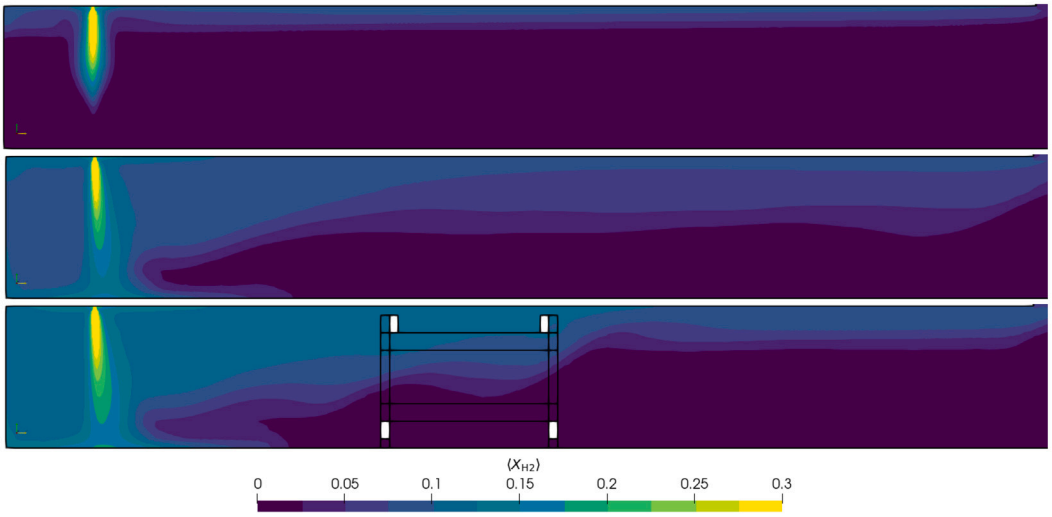

(b) Mean concentrations, $\langle X_{H2} \rangle$, for cases A (top), E (middle) and O2 (bottom).

Fig. 9. Contours of the instantaneous and mean hydrogen volume fractions for cases A (0.086 g/s), E (0.48 g/s) and O2 (0.091 g/s) in a vertical slice at $x = 0$. Contour levels from 0 (dark blue) to 0.3 (yellow) are shown. For case O2, the outline of the obstruction is illustrated by black lines. (For interpretation of the references to color in this figure legend, the reader is referred to the web version of this article.)

Fig. 10 shows the mean volume concentration and streamwise velocity profiles along vertical lines at five different streamwise locations for cases A and E. From $y = 2$ and downstream, the mean flow and concentration fields appear relatively homogeneous in the streamwise direction in both cases.

The gradual concentration gradient of case E is clearly evident. The concentration at the half-height is approximately the average of the floor and ceiling values. For case A, a stratified regime with a pronounced concentration peak near the ceiling is evident.

The streamwise velocity shows that for the lower mass flow, the hydrogen-rich outflow occurs near the ceiling. However, the inflow of air also takes place mainly in the top half of the channel, just below the outflow current. For the higher mass flow of case E, on the other hand, the outflow occupies the entire top half of the channel and the inflow occurs in the bottom half.

The hydrogen outflow constitutes a light-fluid intrusion, and is a part of a gravity-current system [cf., e.g.,56,57], albeit less pronounced than in typical lock-exchange problems. The magnitude of the current increases with increased mass flow of injected hydrogen. This is seen from Fig. 10 and is also found from inspection of data from the other cases. The inner region of the channel (between the jet and the rear wall) acts as an infinite reservoir of hydrogen, continually driving the gravity current.

4.3. The local Froude number and the jet momentum length

The jet Froude number characterizes the hydrogen injection [58] and is included in Table 2. It is given by

$$\mathrm{Fr}_j = \frac{U_j}{\sqrt{g D_j (\rho_{\mathrm{air}} - \rho_{\mathrm{H2}})/\rho_{\mathrm{H2}}}},$$

where U_j and D_j are the (area-averaged) velocity and diameter of the inflow jet, g is the gravitational acceleration (magnitude), and ρ_{H2} and ρ_{air} are the densities of the hydrogen jet and the ambient air, respectively.

Since the Froude number generally relates inertial and gravitational forces, a local and instantaneous Froude number can also be defined from the momentum conservation equation.

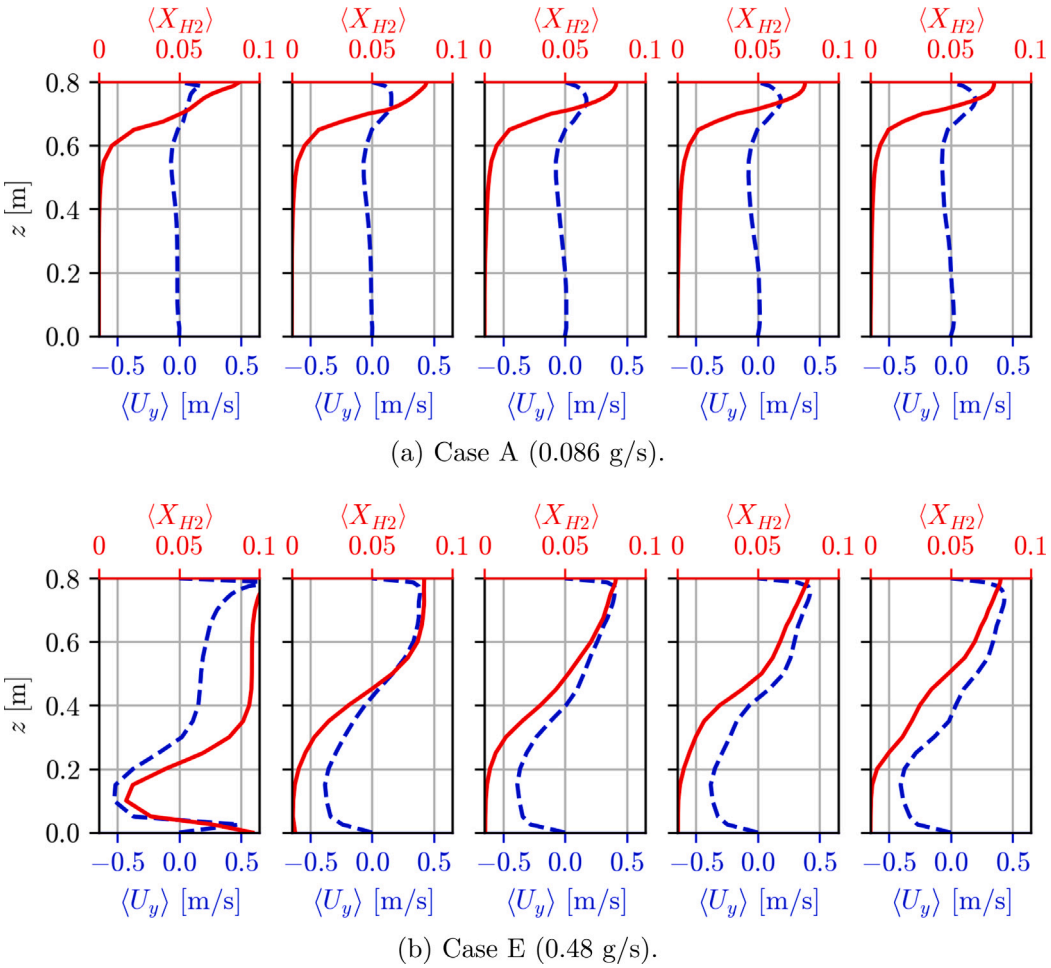

Fig. 10. Vertical profiles of mean hydrogen concentration (solid, red) and streamwise velocity (dashed, blue) at $y = \{1, 2, 3, 4, 5\}$ m (from left to right) in the center of the channel ($x = 0$). (For interpretation of the references to color in this figure legend, the reader is referred to the web version of this article.)

For simplicity, but without loss of generality, we assume steady conditions. Substituting the modified pressure into Eq. (2), the inertial and gravitational force terms can be used to form a Froude number:

$$\mathrm{Fr}^2_{\mathrm{local}} = \frac{|\nabla \cdot (\widetilde{\rho}\widetilde{\mathbf{u}}\widetilde{\mathbf{u}})|}{|\widetilde{\rho}\mathbf{g}|}. \tag{8}$$

Flow regions where $\mathrm{Fr}_{\mathrm{local}} \ll 1$ is dominated by gravitational forces, whereas $\mathrm{Fr}_{\mathrm{local}} \gg 1$ indicates regions with strong inertial effects.

Dimensional analysis can be used to simplify Eq. (8) into a characteristic Froude number, i.e.,

$$\mathrm{Fr}^2_c = \frac{U_c^2(1 + \Delta\rho/\rho_0)}{gL_c}, \tag{9}$$

where U_c and L_c are characteristic velocity and length scales, respectively, $\Delta\rho/\rho$ is a representative relative density difference, and g is the gravitational acceleration magnitude.[7]

Fr_c resembles a common form of the Froude number, only with an additional term, $\Delta\rho U_c^2/\rho_0$, to account for the effects of large density variations. Under the Boussinesq approximation, where $\Delta\rho/\rho_0 \ll 1$ for a chosen reference density, ρ_0, the densimetric Froude number can be derived from a similar ratio of terms from the corresponding momentum equation using a reduced gravity.

Fig. 11 shows contours of the (mean) local Froude number field for cases A, C, and E, along with mean-flow streamlines.

For very low mass flows (case A), the jet (i.e., the momentum-dominated jet region) does not reach the floor of the channel, which is also seen from the zero mean concentrations for sensors 21, 23, and 25 in Fig. 7. For high mass flows (case E), the jet is strong enough to impinge on the channel floor, causing higher concentrations and enhanced mixing in the bottom part of the inner region of the channel. This leads to a "fading box" type concentration field.

The intermediate mass flow (case B) exhibits a jet that barely reaches the floor of the channel; this case has a hydrogen mass flow of 0.15 g/s and yields top-sensor concentrations close to the minimum measurements in Fig. 7.

For cases A and B, it is evident that the "end" of the jet, i.e. where the local flow direction no longer aligns with the flow direction of the downward jet, corresponds well with the transition region where $\langle \mathrm{Fr} \rangle \approx 1$. The local Froude number can thus be used to indicate the penetration distance of the hydrogen jet, i.e., to estimate the jet-momentum length, l_s, used in the identification of the dispersion regime through the Morton number.

Fig. 12 shows the mean Froude number, $\langle \mathrm{Fr} \rangle$, along a vertical line from the inlet to the channel floor for cases A, B, C, E, and G. As expected, the local Froude number near the inlet is of similar order of magnitude as the global Froude number defined based on the jet inlet characteristics, i.e. Fr_j.

The data in Fig. 12 suggests that the mean local Froude number along the center of the downward jet scales as

[7] U_c arises from the more general ΔU scale under the assumption of quiescent ambient fluid, i.e., $\Delta U = U_c - 0$.

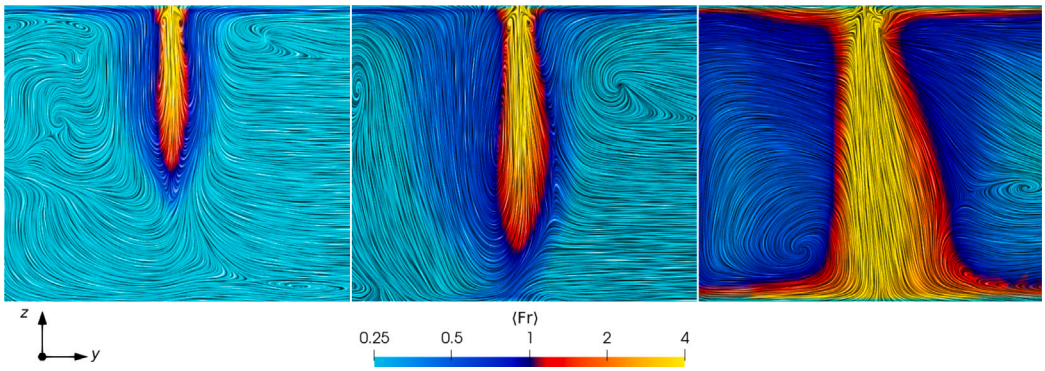

Fig. 11. Mean local Froude number, Eq. (8), in a vertical slice through the H_2 jet (in $x = 0$) for cases A (0.086 g/s), B (0.15 g/s), and E (0.48 g/s). Buoyancy- and momentum-dominated regions are shaded with blue and red-yellow, respectively, as shown by the color bar. The mean flow fields are illustrated by line-integral convolution [59]. (For interpretation of the references to color in this figure legend, the reader is referred to the web version of this article.)

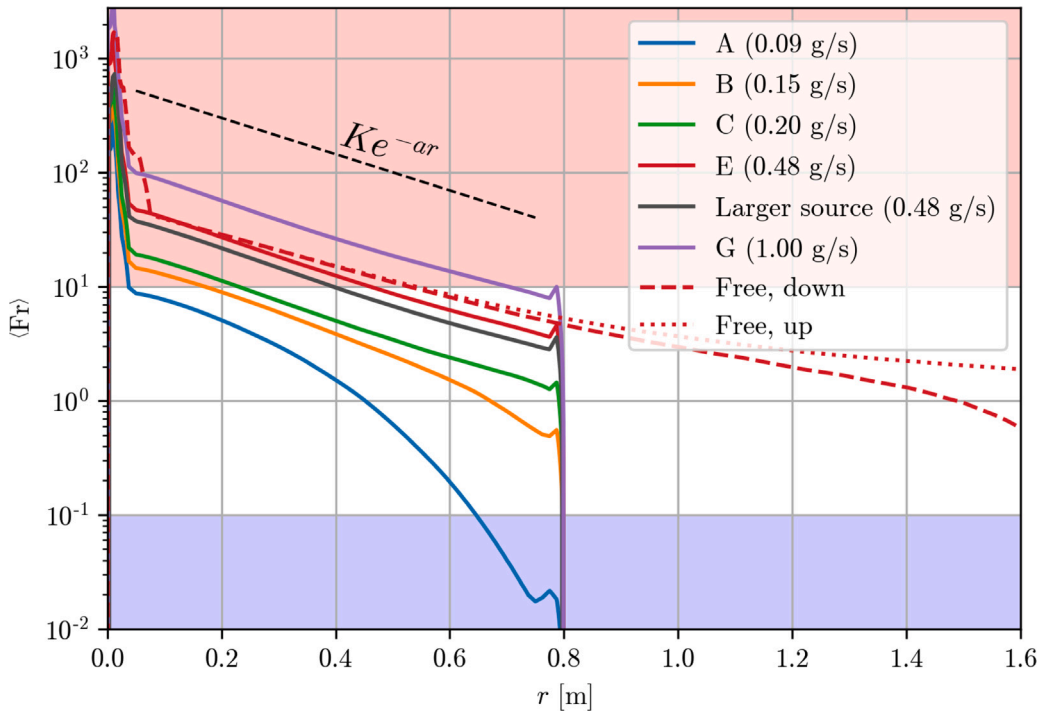

Fig. 12. Log-linear plot of the mean local Froude number along the jet centerline, r. Dashed and dotted lines indicate free-jet simulations with a mass flow of 0.48 g/s. The exponential scaling law with $a = 3.66$ m^{-1} is also shown (black, dashed). Buoyancy- and momentum-dominated regions are shaded with blue and red, respectively. (For interpretation of the references to color in this figure legend, the reader is referred to the web version of this article.)

$$\langle \mathrm{Fr} \rangle (r) = Ke^{-ar}, \tag{10}$$

where r is the distance along the jet centerline and K and a are constants. The only exceptions are cases A and – to some degree – B, in which the jet decays rapidly due to its low initial momentum. These are also the cases where the jet does not reach the channel floor.

Note that a appears to be approximately equal for all the cases where the jet reaches the floor (cases C–H), and even for case B when $r \lesssim 0.6$. This implies (i) that the scaling-law is generally valid in the $\langle \mathrm{Fr} \rangle \gtrsim 1$ regime, and (ii) that a does not depend directly on the jet Froude number (i.e., the jet inlet velocity).

Two additional simulations of free jets with similar injections as case E were carried out to investigate whether increasing the distance to nearby walls would impact the result. For a vertical spacing of 3 m and horizontal wall-distances of 3 m in either direction, both a downward and an upward jet were simulated. The results are included in Fig. 12. Another simulation with twice the jet-orifice area and the same mass flow as case E was also performed, indicating the same value of a as the smaller source of the same mass flow.

Apparently, the mean local Froude number along the centerline of the downward jet in a larger domain adheres to scaling law of Eq. (10), although with a slightly different value of a in, perhaps indicating a minor effect of nearby walls for the other cases. The upward jet follows the same Froude number evolution in the momentum-dominated region, as expected. However, once buoyancy forces are no longer negligible, the behavior of the upward jet differs markedly from the downward case; the mean local Froude number indicates a stretching of the intermediate region in comparison with the downward jet.

The constant of proportionality, K, in Eq. (10) is case-dependent and can be shown to scale linearly with Fr_j (and thus also with the mass flow and jet velocity), i.e., $K = b\mathrm{Fr}_j$ for a constant coefficient b.

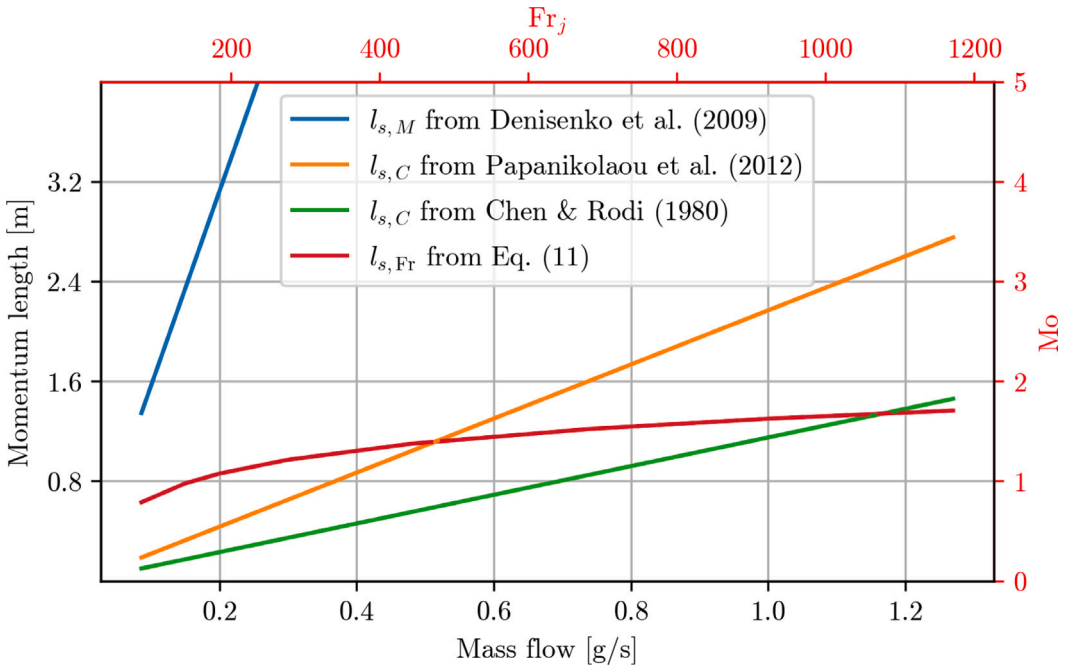

Fig. 13. Estimated momentum lengths. The pair of bottom and left axes (black) shows the physical dimensions, whereas the pair of top and right axes (red) shows the corresponding Morton and jet Froude numbers. (For interpretation of the references to color in this figure legend, the reader is referred to the web version of this article.)

Using the scaling law of Eq. (10), the criterion $\langle \mathrm{Fr} \rangle < \mathrm{Fr}_{\mathrm{thr}}$ can be utilized to estimate a jet penetration distance of a buoyant downward jet, i.e.,

$$l_{s,\mathrm{Fr}} = \frac{1}{a} \ln\left(\frac{b\mathrm{Fr}_j}{\mathrm{Fr}_{\mathrm{thr}}}\right), \tag{11}$$

for a suitable threshold value, $\mathrm{Fr}_{\mathrm{thr}}$. The resulting penetration distances are shown in Fig. 13 for a threshold value of $\mathrm{Fr}_{\mathrm{thr}} = 1$, using $a = 3.66$ m^{-1} and $b = 0.126$ (from curve-fitting the simulation data of cases C, E and G). From the figure, it can be seen that the jet momentum length exceeds the channel height (H = 0.8 m) at a mass flow of 0.17 g/s.

Another common estimate of the momentum length scale is [55,60]

$$l_{s,M} = 0.96\sqrt{\frac{\rho_{\mathrm{air}}}{\rho_{\mathrm{H2}}}} D_j \mathrm{Fr}_j,$$

derived under the assumption of a constant jet entrainment velocity ratio of 0.12 and a circular jet orifice. The Boussinesq assumption is also employed. This estimate, often used with the Morton number [54] of Eq. (7), yields significantly longer jet-penetration distances, as shown in Fig. 13.

From the same figure, it can be seen that the momentum-length estimate of Papanikolaou et al. [20], given by

$$l_{s,C} = X_b \left(\frac{\rho_{\mathrm{H2}}}{\rho_{\mathrm{air}}}\right)^{\frac{1}{4}} D_j \mathrm{Fr}_j,$$

with $X_b = 1$, appears closer to our observed results; it is expected that the transition from "filling box" to "fading box" behavior occurs around Mo = 1, i.e. where the momentum length is similar to the channel height (H = 0.8 m). The functional form of $l_{s,C}$ follows from dimensional analysis, and the original authors [61] found $X_b = 0.53$ as the end of the pure-jet regime. However, they identify a wide intermediate range, $0.53 \leq X_b \leq 5.3$, for which the jet is transitional from momentum-dominated to buoyancy-dominated. Chen and Rodi [61] also use the Boussinesq approximation in their derivation, noting that exact jet self-similarity cannot exist otherwise.

A smoother "fading box" concentration gradient can be expected for the higher mass flows (as Mo $\gg$ 1). However, for mass flows $\leq$ 0.2 g/s, our concentration data (Fig. 7) appears to show a rather clear stratification, indicating Mo < 1. This is corroborated by Figs. 9 and 10, which show a distinct concentration layer close to the ceiling for case A. Also, it is evident from Fig. 11 that the jet in case A never reaches the channel floor, also suggesting that Mo < 1 here. From the data presented in this paper, it seems likely that the Morton number exceeds unity around a mass flow of 0.15 to 0.2 g/s (i.e., $\mathrm{Fr}_j \approx 150$).

Fig. 13 shows that with $l_{s,M}$ as the momentum length scale, Mo > 1 for all our cases, clearly not in line with the concentration data. The two versions of $l_{s,C}$ seem more reasonable, even if they predict momentum lengths apparently a bit too short; $X_b = 1$ [20] implies Mo = 1 at a mass flow of approximately 0.4 g/s.

Using Eq. (11) as the momentum length scale in Eq. (7), the Morton numbers for our cases, $\mathrm{Mo}_{\mathrm{Fr}} = l_{s,\mathrm{Fr}}/H$, correspond very well with the dispersion regime observed for the different cases. For cases A and B, $\mathrm{Mo}_{\mathrm{Fr}} < 1$, and for cases C–H, $\mathrm{Mo}_{\mathrm{Fr}} > 1$. Case B and C exhibit $\mathrm{Mo}_{\mathrm{Fr}} \approx 1$, and this is also where we observe the transition from the "filling box' to the 'fading box' regime in the channel.

All the linear models employ the Boussinesq approximation and assumes a "universal" entrainment velocity ratio, which implies that the jet-momentum length is independent of jet direction. Differences in density scaling and the exact choice of the end of the momentum-driven jet regime (based on empirical data) lead to different gradients. Our proposed model, $l_{s,\mathrm{Fr}}$, is functionally different and only valid for downward jets.

4.4. Estimated hazard predictions

Hydrogen is considered flammable in air for volume concentrations between 4 and 75%. If ignited, an upper bound for the amount of hydrogen that undergoes combustion in the channel can be found by integrating the mass of hydrogen in the flammable regions. Moreover, assuming stoichiometry, an upper bound for the energy release can be found.

Fig. 14 shows the flammable normal volume and predicted maximum energy release from stoichiometric combustion of flammable hydrogen in the channel for our different simulations. The heat of combustion is taken as 3.01 MJ/m^3 [62, p. 5.16].

The curves for the flammable volume and released heat have identical shapes, since they are linearly related; the numerical values are

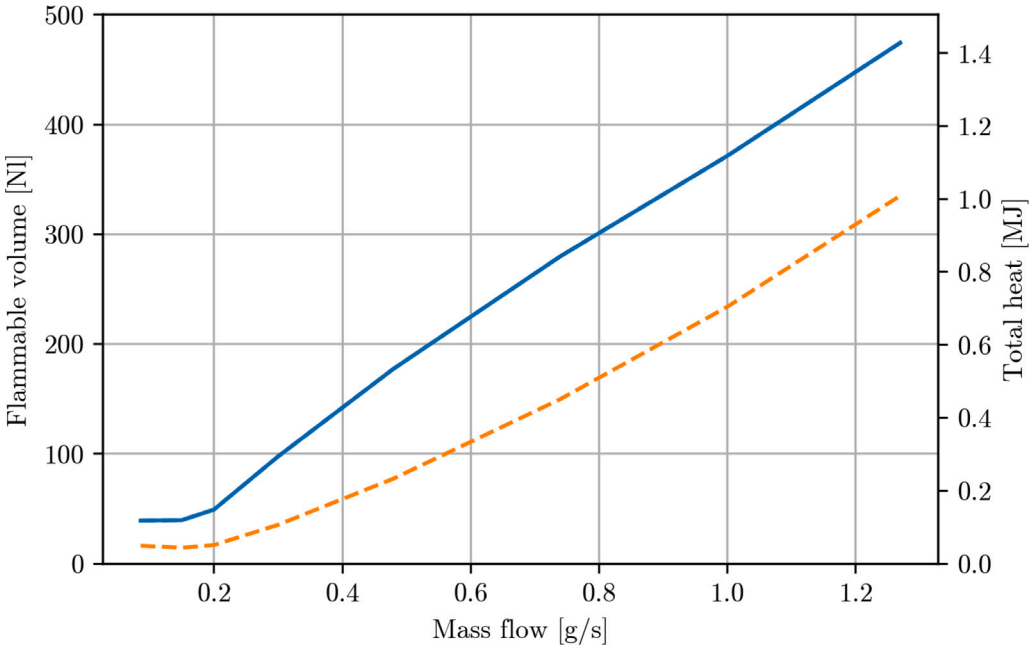

Fig. 14. Total flammable volume (blue, solid line) and Q8 (orange, dashed line) of H_2 in the channel (left axis), with the maximum total heat released from complete combustion (right axis), assuming stoichiometry, for different injection rates. (For interpretation of the references to color in this figure legend, the reader is referred to the web version of this article.)

shown on the left and right vertical axes of the figure. For mass flows higher than 0.2 g/s, the increase in flammable mass and resulting released heat appears to increase approximately linearly.

The "equivalent cloud" concept is often used to estimate pressure loads from vapor cloud explosions (VCEs) for inhomogeneous gas clouds. The flammable volume can in principle be used, but it is very conservative. The Q8 cloud metric incorporates the relative volume expansion in the gas cloud. It is considered more suited to hydrogen explosions in confined/congested spaces [63]. With Q8, the gas volume used in the equivalent (homogeneous) cloud is calculated as [64]

$$V_{Q8} = \frac{1}{E_{\max}} \int_V Y_{\mathrm{H2}} E\left(Y_{\mathrm{H2}}\right) \mathrm{d}V$$

where E is the (local) volume expansion of the mixture during combustion, given the mixture fraction of hydrogen, and $E_{\max}$ is the maximum volume expansion possible. We computed E by means of the Cantera library for Python and the GRI-MECH 3.0 mechanism [see, e.g.,43]

Fig. 14 also shows the Q8 volumes for the (quasi-)steady states under the different injected mass flows in our semi-open channel. According to Hansen et al. [63], Q8 is typically around two-thirds of the flammable volume for hydrocarbon gas clouds. From our data, this also seems to be the case for hydrogen clouds.

5. Concluding remarks

In this work, we have simulated dispersion from high-Reynolds number subsonic hydrogen jets in a long channel and compared the resulting concentration fields to experimental measurements. In general, *buoyantReactingFoam* reliably predicts the hydrogen concentration levels in the channel for a range of injected mass flows (0.086 to 1.27 g/s), including cases with geometric obstructions in the channel. A statistical evaluation of all cases with reference data yields $0.04 < |\mathrm{FB}| < 0.225$ and $0.025 < \mathrm{NMSE} < 0.105$. Simulated jets with very low or high mass flows exhibit the largest differences between experimental and numerical results.

The results indicate that as the rate of hydrogen injection increases, the dispersion regime changes from a stratified "filling box" regime to a more well-mixed "fading box" regime. In our geometry, this transition occurs around a hydrogen mass flow of 0.15 g/s. The transition is evident in changes in the structure of both the concentration and flow fields and thus also affects derived quantities like equivalent-cloud estimates.

The Morton number supposedly quantifies the transition between the two dispersion regimes by scaling the jet momentum length with the distance to the nearest wall opposite the jet orifice. This is highly dependent on the choice of the jet momentum length scale, and we find that common existing estimates are lacking due to inherent assumptions; most importantly, the Boussinesq approximation is not generally valid for high-momentum hydrogen jets, due to the significant density gradients involved. Furthermore, the constant-entrainment assumption only holds in the momentum-dominated regime. In this paper, we have proposed a new estimate for the momentum length scale, suitable for non-Boussinesq light-fluid downward jets.

It would be of interest to conduct further simulations in different channel geometries and with different jet directions to further investigate the model coefficients of our proposed length scale. Moreover, the experimental reference data contains pressure records from hydrogen deflagration in the channel. Investigating numerical simulations of such inhomogeneous vapor-cloud explosions within the OpenFOAM framework would also be valuable and is planned in a follow-up study.

CRediT authorship contribution statement

H.E. Fossum: Writing – review & editing, Writing – original draft, Methodology, Formal analysis, Data curation, Conceptualization. **E. Åkervik:** Writing – review & editing, Methodology, Formal analysis, Data curation, Conceptualization. **M. Henriksen:** Writing – review & editing, Methodology, Formal analysis, Data curation, Conceptualization. **D. Bjerketvedt:** Writing – review & editing, Methodology, Formal analysis, Data curation, Conceptualization.

Declaration of competing interest

The authors declare that they have no known competing financial interests or personal relationships that could have appeared to influence the work reported in this paper.

Acknowledgments

This work was performed within MoZEES, a Norwegian Center for Environment-friendly Energy Research (FME) co-sponsored by the Research Council of Norway (project number 257653) and 40 partners from research, industry, and the public sector. The authors would also like to thank the article reviewers for valuable feedback.

References

[1] Clarke J, Dettmer W, Wen J, Ren Z. Cryogenic hydrogen jet and flame for clean energy applications: Progress and challenges. Energies 2023;16. http://dx.doi.org/10.3390/en16114411.
[2] Abohamzeh E, Salehi F, Sheikholeslami M, Abbassi R, Khan F. Review of hydrogen safety during storage, transmission, and applications processes. J Loss Prev Process Ind 2021;72. http://dx.doi.org/10.1016/j.jlp.2021.104569.
[3] Li Y, Jiang J, Yu Y, Zhang Q. Numerical simulation of dispersion and distribution behaviors of hydrogen leakage in the garage with a crossbeam. Simulation 2019;95. http://dx.doi.org/10.1177/0037549718825303.
[4] Gallego E, Migoya E, Martin-Valdepenas J, Crespo A, Garcia J, Venetsanos A, et al. An intercomparison exercise on the capabilities of CFD models to predict distribution and mixing of H_2 in a closed vessel. Int J Hydrog Energy 2007;32(13):2235–45.
[5] Papanikolaou E, Venetsanos A, Heitsch M, Baraldi D, Huser A, Pujol J, et al. HySafe SBEP-V20: Numerical studies of release experiments inside a naturally ventilated residential garage. Int. J. Hydrog. Energy 2010;35(10):4747–57.
[6] Giannissi S, Shentsov V, Melideo D, Cariteau B, Baraldi D, Venetsanos A, et al. CFD benchmark on hydrogen release and dispersion in confined, naturally ventilated space with one vent. Int J Hydrog Energy 2015;40(5):2415–29.
[7] Bernard-Michel G, Saikali E, Sergent A, Tenaud C. Comparisons of experimental measurements and large eddy simulations for a helium release in a two vents enclosure. Int J Hydrog Energy 2019;44(17):8935–53.
[8] Tolias I, Giannissi S, Venetsanos A, Keenan J, Shentsov V, Makarov D, et al. Best practice guidelines in numerical simulations and CFD benchmarking for hydrogen safety applications. Int J Hydrog Energy 2019;44. http://dx.doi.org/10.1016/j.ijhydene.2018.06.005.
[9] Giannissi SG, Tolias IC, Melideo D, Baraldi D, Shentsov V, Makarov D, et al. On the CFD modelling of hydrogen dispersion at low-Reynolds number release in closed facility. Int J Hydrog Energy 2021;46(57):29745–61.
[10] Zhang X, Wang Q, Hou X, Li Y, Miao Y, Li K, et al. Numerical analysis of the hydrogen dispersion behavior in different directions in a naturally ventilated space. Appl Sci 2021;11. http://dx.doi.org/10.3390/app11020615.
[11] Li Y, Hou X, Wang C, Wang Q, Qi W, Li J, et al. Modeling and analysis of hydrogen diffusion in an enclosed fuel cell vehicle with obstacles. Int J Hydrog Energy 2022;47(9):5745–56.
[12] Xu Q, Chen G, Xie M, Li X, Zhao Y, Su S, et al. Experimental and numerical studies on hydrogen leakage and dispersion evolution characteristics in space with large aspect ratios. J Clean Prod 2024;438:140467.
[13] Birch A, Brown D, Dodson M, Swaffield F. The structure and concentration decay of high pressure jets of natural gas. Combust. Sci. Technol. 1984;36(5–6):249–61.
[14] Makarov D, Molkov V. Plane hydrogen jets. Int J Hydrog Energy 2013;38(19):8068–83.
[15] Li X, Chen Q, Chen M, He Q, Christopher DM, Cheng X, et al. Modeling of underexpanded hydrogen jets through square and rectangular slot nozzles. Int. J. Hydrog. Energy 2019;44(12):6353–65.
[16] Birch A, Hughes D, Swaffield F. Velocity decay of high pressure jets. Combust. Sci. Technol. 1987;52(1–3):161–71.
[17] Ewan BC, Moodie K. Structure and velocity measurements in underexpanded jets. Combust. Sci. Technol. 1986;45(5–6):275–88.
[18] Yüceil KB, Ötügen MV. Scaling parameters for underexpanded supersonic jets. Phys Fluids 2002;14(12):4206–15.
[19] Molkov V, Makarov D, Bragin M. Physics and modelling of underexpanded jets and hydrogen dispersion in atmosphere. In: Physics of extreme states of matter-2009. Russian Academy of Sciences; 2009, p. 146–9.
[20] Papanikolaou E, Baraldi D, Kuznetsov M, Venetsanos A. Evaluation of notional nozzle approaches for CFD simulations of free-shear under-expanded hydrogen jets. Int J Hydrog Energy 2012;37(23):18563–74.
[21] Li X, Chowdhury BR, He Q, Christopher DM, Hecht ES. Validation of two-layer model for underexpanded hydrogen jets. Int J Hydrog Energy 2021;46. http://dx.doi.org/10.1016/j.ijhydene.2020.08.204.
[22] Yu X, Wang C, He Q. Numerical study of hydrogen dispersion in a fuel cell vehicle under the effect of ambient wind. Int J Hydrog Energy 2019;44. http://dx.doi.org/10.1016/j.ijhydene.2019.03.234.
[23] Qian J-y, Li X-j, Gao Z-x, Jin Z-j. A numerical study of hydrogen leakage and diffusion in a hydrogen refueling station. Int J Hydrog Energy 2020;45. http://dx.doi.org/10.1016/j.ijhydene.2020.03.140.
[24] Hussein H, Brennan S, Molkov V. Dispersion of hydrogen release in a naturally ventilated covered car park. Int J Hydrog Energy 2020;45. http://dx.doi.org/10.1016/j.ijhydene.2020.06.194.
[25] Xiao J, Travis J, Breitung W. Non-Boussinesq integral model for horizontal turbulent buoyant round jets. Sci Technol Nucl Install 2009;2009.
[26] Li X, Hecht ES, Christopher DM. Validation of a reduced-order jet model for subsonic and underexpanded hydrogen jets. Int J Hydrog Energy 2016;41(2):1348–58.
[27] Sathiah P, Dixon CM. Numerical modelling of release of subsonic and sonic hydrogen jets. Int J Hydrog Energy 2019;44(17):8842–55.
[28] Winters W, Houf W. Simulation of small-scale releases from liquid hydrogen storage systems. Int J Hydrog Energy 2011;36(6):3913–21.
[29] Keenan J, Makarov D, Molkov V. Modelling and simulation of high-pressure hydrogen jets using notional nozzle theory and open source code OpenFOAM. Int J Hydrog Energy 2017;42(11):7447–56.
[30] Middha P, Hansen OR, Grune J, Kotchourko A. CFD calculations of gas leak dispersion and subsequent gas explosions: Validation against ignited impinging hydrogen jet experiments. J Hard Mater 2010;179(1–3):84–94.
[31] Henriksen M, Fossum H, kervik EA, Bjerketvedt D. Experiments and simulations of hydrogen dispersion in a 6-meter-long channel. In: Proceedings of the 15th international symposium on hazards, prevention and mitigation of industrial explosions. Naples, Italy; 2024, http://dx.doi.org/10.5281/zenodo.12515711.
[32] Henriksen M, Hannibal F, Åkervik E, Bjerketvedt D. Experimental data of hydrogen dispersion in an open-ended rectangular channel. University of South-Eastern Norway; 2024, http://dx.doi.org/10.23642/usn.26117989, URL https://usn.figshare.com/account/articles/26117989.
[33] Greenshields C, Weller H. Notes on computational fluid dynamics: General principles. Reading, UK: CFD Direct Ltd; 2022.
[34] Åkervik E, Fossum HE, Henriksen M, Bjerketvedt D. Measurements of hydrocarbon flame propagation in a channel. Technical 21/00790, Norwegian Defence Research Establishment; 2021, URL https://publications.ffi.no/nb/item/asset/dspace:7076/21-00790.pdf.
[35] Kim J, Jung E, Kang S. Large eddy simulation of hydrogen dispersion from leakage in a nuclear containment model. Int J Hydrog Energy 2015;40(35):11762–70.
[36] Sharma PK, Gera B, Singh R. Application of RANS and LES based CFD to predict the short and long term distribution and mixing of hydrogen in a large enclosure. CFD Lett 2011;3(1):18–31.
[37] Koutsourakis N. Evaluation of an LES code against a hydrogen dispersion experiment. CFD Lett 2012;4(4):225–36.
[38] Lin C, Ooka R, Kikumoto H, Sato T, Arai M. CFD simulations on high-buoyancy gas dispersion in the wake of an isolated cubic building using steady RANS model and LES. Build Environ 2021;188:107478.
[39] Xie H, Makarov D, Kashkarov S, Molkov V. CFD simulations of hydrogen tank fuelling: Sensitivity to turbulence model and grid resolution. Hydrogen 2023;4(4):1001–21.
[40] Nicoud F, Ducros F. Subgrid-scale stress modelling based on the square of the velocity gradient tensor. Flow Turbul Combust 1999;62. http://dx.doi.org/10.1023/a:1009995426001.
[41] Versteeg H, Malalasekera W. An introduction to computational fluid dynamics: The finite volume method. Pearson Education Limited; 2007, URL https://books.google.no/books?id=RvBZ-UMpGzIC.
[42] McBride BJ, Gordon S, Reno MA. Coefficients for calculating thermodynamic and transport properties of individual species. Technical NASA TM-4513, NASA; 1993, p. 94, URL https://ntrs.nasa.gov/api/citations/19940013151/downloads/19940013151.pdf.
[43] Henriksen M, Bjerketvedt D. mech2Foam - Generating transport, combustion, and thermodynamic properties for the CFD solver XiFoam. University of South-Eastern Norway; 2021, http://dx.doi.org/10.23642/USN.13721134.V4, URL https://usn.figshare.com/articles/software/Generating_thermodynamic_and_combustion_properties_for_CFD_mech2Foam/13721134/4.
[44] Smith GP, Golden DM, Frenklach M, Moriarty NW, Eiteneer B, Goldenberg M, et al. GRI-MECH 3.0. 1999, URL http://combustion.berkeley.edu/gri-mech/version30/text30.html.
[45] Spalding DB. A single formula for the "Law of the Wall". J Appl Mech 1961;28. http://dx.doi.org/10.1115/1.3641728.
[46] Wong GS. Handbook of the speed of sound in real gases. Academic Press; 2002.
[47] Geurts BJ. Interacting errors in large-eddy simulation: a review of recent developments. J Turbul 2006;7(55):N55.
[48] Wyngaard J. Turbulence in the atmosphere. Cambridge University Press; 2010, URL https://books.google.no/books?id=YLeBN1qYn-0C.
[49] Wingstedt EMM, Vartdal M, Reif P. Large-eddy simulations of dense-gas dispersion within a high-Reynolds number turbulent boundary layer. Phys Fluids 2017;29(9).
[50] Pope SB. Ten questions concerning the large-eddy simulation of turbulent flows. New J Phys 2004;6(1):35.
[51] Chang JC, Hanna SR. Air quality model performance evaluation. Meteorol Atmos Phys 2004;87. http://dx.doi.org/10.1007/s00703-003-0070-7.
[52] Hanna S, Chang J, Strimaitis D. Hazardous gas model evaluation with field observations. Atmos Environ A. 1993;27(15):2265–85. http://dx.doi.org/10.1016/0960-1686(93)90397-H, URL https://www.sciencedirect.com/science/article/pii/096016869390397H.

[53] Henriksen M, Vaagsaether K, Lundberg J, Forseth S, Bjerketvedt D. Numerical study of premixed gas explosion in a 1-m channel partly filled with 18650 cell-like cylinders with experiments. J Loss Prev Process Ind 2022;77:104761. http://dx.doi.org/10.1016/j.jlp.2022.104761, URL https://www.sciencedirect.com/science/article/pii/S0950423022000389.

[54] Denisenko V, Kirillov I, Korobtsev S, Nikolaev I. Hydrogen-air explosive envelope behaviour in confined space at different leak velocities. In: Proceedings of international conference on hydrogen safety. 2009, URL https://www.h2knowledgecentre.com/content/conference423.

[55] De Stefano M, Rocourt X, Sochet I, Daudey N. Hydrogen dispersion in a closed environment. Int J Hydrog Energy 2019;44(17):9031–40.

[56] Gröbelbauer H, Fannelø p T, Britter R. The propagation of intrusion fronts of high density ratios. J Fluid Mech 1993;250:669–87.

[57] Härtel C, Meiburg E, Necker F. Analysis and direct numerical simulation of the flow at a gravity-current head. Part 1. Flow topology and front speed for slip and no-slip boundaries. J Fluid Mech 2000;418:189–212.

[58] Schefer RW, Houf WG, Williams T. Investigation of small-scale unintended releases of hydrogen: momentum-dominated regime. Int J Hydrog Energy 2008;33(21):6373–84.

[59] Cabral B, Leedom LC. Imaging vector fields using line integral convolution. In: Proceedings of the 20th annual conference on computer graphics and interactive techniques. 1993, p. 263–70.

[60] Hunt G, Kaye N. Virtual origin correction for lazy turbulent plumes. J Fluid Mech 2001;435:377–96.

[61] Chen CJ, Rodi W. Vertical turbulent buoyant jets: A review of experimental data. Oxford: Pergamon Press; 1980.

[62] van den Bosch C, Weterings R. Methods for the calculation of physical effects (TNO Yellow Book). The Netherlands: TNO, The Hague; 1997.

[63] Hansen OR, Gavelli F, Davis SG, Middha P. Equivalent cloud methods used for explosion risk and consequence studies. J Loss Prev Process Ind 2013;26(3):511–27.

[64] Tam VH, Tan F, Savvides C. A critical review of the equivalent stoichiometric cloud model Q9 in gas explosion modelling. Eng 2021;2(2):156–80.